Trap characterization in ultra-wide bandgap $Al_{0.65}Ga_{0.4}N/Al_{0.4}Ga_{0.6}N$ MOSHFET's with ZrO_2 gate dielectric using optical response and cathodoluminescence

Cite as: Appl. Phys. Lett. **115**, 213502 (2019); https://doi.org/10.1063/1.5125776 Submitted: 28 August 2019 . Accepted: 09 November 2019 . Published Online: 19 November 2019

Mohi Uddin Jewel ⁽¹⁾, Md Didarul Alam, Shahab Mollah ⁽¹⁾, Kamal Hussain, Virginia Wheeler ⁽¹⁾, Charles Eddy, Mikhail Gaevski, Grigory Simin, MVS Chandrashekhar, and Asif Khan ⁽¹⁾







ARTICLES YOU MAY BE INTERESTED IN

Photocurrents in GaN-based HEMTs: Theoretical model and experimental results Applied Physics Letters 115, 213505 (2019); https://doi.org/10.1063/1.5128825

Enhance stable coupling region of a high-Q WGM up to micrometer Applied Physics Letters 115, 211104 (2019); https://doi.org/10.1063/1.5121452

Self-cleaning organic solar cells based on micro/nanostructured haze films with optical enhancement effect

Applied Physics Letters 115, 213902 (2019); https://doi.org/10.1063/1.5129588









Trap characterization in ultra-wide bandgap Al_{0.65}Ga_{0.4}N/Al_{0.4}Ga_{0.6}N MOSHFET's with ZrO₂ gate dielectric using optical response and cathodoluminescence

Cite as: Appl. Phys. Lett. **115**, 213502 (2019); doi: 10.1063/1.5125776 Submitted: 28 August 2019 · Accepted: 9 November 2019 · Published Online: 19 November 2019 · Publisher error corrected: 20 November 2019







Mohi Uddin Jewel, ^{1,a)} D Md Didarul Alam, Shahab Mollah, D Kamal Hussain, Virginia Wheeler, D Charles Eddy, Mikhail Gaevski, Grigory Simin, MVS Chandrashekhar, and Asif Khan D

AFFILIATIONS

¹Department of Electrical Engineering, University of South Carolina, Columbia, South Carolina 29201, USA ²U.S. Naval Research Laboratory, Washington, DC 20375, USA

ABSTRACT

Ultrawide bandgap (UWBG) AlGaN-channel metal-oxide-semiconductor heterostructure field-effect transistors (MOSHFETs) with a ZrO $_2$ gate dielectric achieve peak current in excess of 0.4 A/mm and current ON/OFF ratios >10 6 with subthreshold swings as low as 110 mV/decade. These devices have strong potential for use in power and radio frequency electronics or as true solar-blind photodetectors. In this work, we present the photoresponse analysis in UWBG AlGaN MOSHFETs. Persistent photoconductivity with the decay time above 10 minutes can be quenched by illuminating with strong UV light at 365 nm and 254 nm, suggesting deep traps to be responsible for this behavior. Upon correlating the optical response under various illumination conditions with cathodoluminescence of these devices, we identified two key trap levels at \sim 2.48 \pm 0.14 eV and 3.76 \pm 0.06 eV, controlling the slow response time. By depth-profiling using cathodoluminescence, these traps are identified to be at the AlN/AlGaN interface at the back of the device, due to partial relaxation from the lattice mismatch between AlN and Al_{0.4}Ga_{0.6}N.

Published under license by AIP Publishing. https://doi.org/10.1063/1.5125776

Ultrawide bandgap (UWBG) materials, with a bandgap, E_g > 4.5 eV, such as diamond, Ga₂O₃, and AlGaN, have emerged as candidates for electronic and optoelectronic devices capable of operating in extreme environments, such as in nuclear power plants,² electric vehicles,³ and compact solid-state converters.⁴ The UWBG suppresses thermal carrier generation, reducing leakage current,⁵ and enabling high temperature operation without active cooling. This could potentially reduce the size, weight, and cost of such systems.⁶ Over the past decade, the UWBG $Al_xGa_{1-x}N$ (x ≥ 0.4) has found applications in deep ultraviolet (DUV) light emitting diodes (LEDs) and is a compelling candidate for next generation of power devices and solar-blind photodetectors.^{3,8} On the basis of the Baliga Figure of Merit, Chow and Tyagi have argued the best possible Al_xGa_{1-x}N power devices for Al-mole fractions of \sim 0.6–0.7 owing to their potentially large critical breakdown field arising from the UWBG. However, it is challenging to form contacts to UWBG materials, limiting the currents for power

Our group recently demonstrated 10-13 high electron mobility transistors (HEMTs, a.k.a. HFETs) based on Al_{0.85}Ga_{0.15}N/Al_{0.65}Ga_{0.35}N, with peak currents > 0.2 A/mm, and $Al_{0.65}Ga_{0.35}N/Al_{0.4}Ga_{0.6}N$ with peak currents > 0.5 A/mm. These devices had a minimal drop in peak current for a temperature range of room temperature to 200 °C and a breakdown voltage >600 V. The device performance was further improved by incorporating SiO₂¹¹ and high-k gate-dielectrics, ¹² which increased the ON/OFF ratio. UWBG HFETs and metal-oxide-semiconductor heterostructure field-effect transistors (MOSHFETs) can also be used as true-solar-blind photodetectors with the internal gain due to current amplification. 8,14 However, persistent photocurrent (PPC) is a serious issue affecting the performance in III-N devices, 15 which leads to significant degradation in the noise performance, and speed of HFETbased detectors.¹⁶ The PPC can result from dislocations and deep level defects in the device, which lead to carrier trapping. The deep traps prolong the lifetime of the photogenerated carriers and increase responsivity at the expense of slower response times. Therefore, it is crucial to

a) Author to whom correspondence should be addressed: mjewel@email.sc.edu

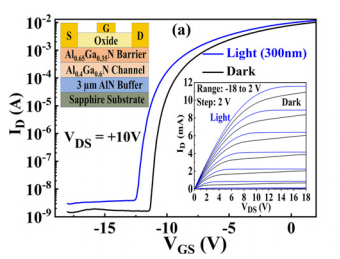
locate the trap states and their spectral position to improve the performance of UWBG AlGaN photodetectors.

Photoresponsivity and luminescence are powerful techniques for studying trapping effects in III-N materials¹⁷ with a spectral resolution. When combined with a scanning technique, such as cathodoluminescence (CL) in a scanning electron microscope (SEM), these techniques can provide both lateral and vertical (tuned by electron beam energy) spatial information. In this paper, we characterize the photoresponse and luminescence of ZrO₂/Al_{0.65}Ga_{0.35}N/Al_{0.4}Ga_{0.6}N MOSHFETs to identify the device regions responsible for PPC. This information can potentially enable defect management in AlGaN photodetectors to achieve both higher responsivity and faster response.

Epitaxial layers were grown by pulsed metalorganic chemical vapor deposition (MOCVD) on a 3 μm thick AlN buffer/sapphire template. The off axis (102) X-ray peak linewidth for the AlN buffers was \sim 330 arc secs, giving an estimated overall defect-density close to (1-3) \times 10 8 cm $^{-2}$. 18 The device consists of 0.5 μ m-thick Al $_{0.4}$ Ga $_{0.6}$ N channel and 300 Å-thick n-Al_{0.65}Ga_{0.35}N barrier layers. Only the barrier layer was silicon doped with a carrier concentration of approximately 4-6 $\times 10^{18} \,\mathrm{cm}^{-3}$ measured by capacitance-voltage. Using the eddy current method, the sheet resistance (R_{sh}) value was measured to be 1900 Ω/\Box , which is consistent with the values extracted from the transmission line method (TLM). The barrier layer in our work was Al_{0.65}Ga_{0.35}N as good Ohmic contact formation is well-understood through UV LED work, 19,20 and our recent demonstration of >0.5 A/mm in this AlGaN composition.¹² The lowest contact resistance reported in the literature for high-Al AlGaN transistors was for our doped Al_{0.65}Ga_{0.35}N barrier. For a HEMT structure, the mole fraction difference should be as large as possible without cracking through strain relief, typically 0.15-0.25. Therefore, we selected Al_{0.4}Ga_{0.6}N as the channel layer.

Device processing started with mesa isolation using Cl₂-based Inductively Coupled Plasma Reactive Ion-etching (ICP-RIE) followed by ohmic-contact formation. E-beam evaporation was used to deposit the Zr/Al/Mo/Au (150/1000/400/300 Å) source/drain ohmic contact metal stack followed by rapid thermal annealing (RTA) at 950 °C for 30 s under N₂. Ohmic contacts were achieved with the specific resistance as low as 1.6 Ω mm. Thermal atomic layer deposition (ALD) of the 100 Å ZrO₂ film on the as-received device was conducted using a Veeco CNT Savannah 200 system at 200 °C with tetrakis(dimethylamido)zirconium (IV) (TDMAZ) and de-ionized water precursors. The TDMAZ precursor was heated to 75 °C to achieve an optimized linear growth rate of 0.7 Å/cycle. The deposition was initiated with 15 water pulses prior to the typical AB pulsing sequence to deposit the gate dielectric to ensure saturation of hydroxyl groups at the AlGaN surface required for conformal ALD nucleation. Ni/Au (1000 Å/2000 Å) was used as the gate metal [Fig. 1(a), inset]. Similar processes were carried out to fabricate HFETs from a piece of the same wafer with no gate dielectric and 300 nm silicon nitride (SiN_x) passivation for use as the control HFET structure. Finally, we also fabricated Al_{0.26}Ga_{0.74}N (30 nm)/GaN (3 µm) Schottky-gate HEMTs using the same fabrication procedures for additional control structures (supplementary material).

Gated transmission line model (GTLM) transistor structures were used to measure C-V characteristics and sheet and contact resistances and separate the effects related to the regions under and outside the gate. In the GTLM structures, the gate lengths varied from 10 μ m to 100 μ m. The lengths of the gate-source and gate-drain access



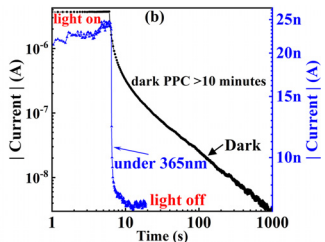


FIG. 1. (a) Transfer characteristics of a $\rm ZrO_2$ -gated $\rm Al_{0.65}Ga_{0.4}N/Al_{0.4}Ga_{0.6}N$ MOSHFET under dark and 300 nm illumination (the inset shows the device structure and output characteristics under the same conditions). (b) Decay transients under dark and 365 nm illumination.

regions were kept constant at $L_{GS}=L_{GD}=10~\mu m$ with a gate-width of $W_G=200~\mu m$. For our study, we also used MOSHFETs with the gate lengths of $L_G=1.8~\mu m$, $L_{GS}=2~\mu m$, and $L_{GD}=7~\mu m$ and $W_G=100~\mu m$. The I-V characteristics ($I_D\text{-}V_{GS}$ and $I_D\text{-}V_{DS}$) were measured using an Agilent 4155C parameter analyzer, while the C-V measurements were done using an HP 4284A LCR Meter. A Xenon lamp, coupled with a monochromator, was used as a photoexcitation light source along with bright sub-bandgap 60 W, 365 nm ($hv < E_g$ of $Al_{0.4}Ga_{0.6}N$), and above bandgap 254 nm ($hv > E_g$ of $Al_{0.4}Ga_{0.6}N$) UV light to identify the main mechanism for PPC.

Carrier trapping was forced in the devices to obtain the photoionization spectra, using the technique described by Klein et al. 17 Dark $I_D\text{-}V_{DS}$ curves were recorded by sweeping the drain voltage from 0 to up to 40 V at $V_{GS} = -4$ V. Before recording the dark I_D - V_{DS} curves, the devices were "reset" using a strong 254 nm UV illumination and then by turning them off. Device I-V curves under illumination with light wavelengths ranging from 250 nm to 750 nm were measured, and then the photocurrent was calculated as the difference between currents under illumination and in the dark. The photocurrents were recorded using illumination from the bottom (through the substrate) of the structure to avoid shadowing from the gate metal. The response function associated with traps for $250 \text{ nm} \le \lambda \le 700 \text{ nm}$ was determined from these measurements. CL spectra were measured as a function of wavelength and e-beam energy (depth profiling) using an SEM equipped with a parabolic mirror spectrometer. The strain and lattice mismatch of the epilayers were characterized by triple-axis high-resolution X-ray diffraction (HRXRD) Reciprocal Space Lattice Map (RSLM) measurements around the asymmetric (105) plane.

The DC characteristics of a 60 μ m × 200 μ m GTLM element are presented in Fig. 1(a) in the dark and under 300 nm illumination. The 60 μ m long gate device is selected to demonstrate the illumination effects with a reasonably low off-state gate leakage (2.7 × 10⁻⁸ A/mm). The device had a threshold voltage (V_{th}) of −10.3 V, a maximum drain current of 0.08 A/mm, an ON/OFF ratio > 10⁶, and a subthreshold slope (SS) of 200 mV/decade at V_{DS} = +10 V. The calculated field effect electron mobility $\mu_{\rm n}$ from the $\sqrt{I_D}$ vs V_{GS} curve using saturation currents $\sqrt{I_D} = \sqrt{\frac{W_G}{2I_G}} \mu_{\rm n} C_G (V_{GS} - V_{th})$ is estimated to be ~245 cm²/Vs from the well-behaved $\sqrt{I_D}$ vs V_{GS} at low currents, where the voltage drop across the contact and access region resistances is negligible. The output curves show well-behaved saturation up to 18 V.

To demonstrate the photoresponse of this device, the I-V characteristics were measured with incident light wavelengths of 250–700 nm.

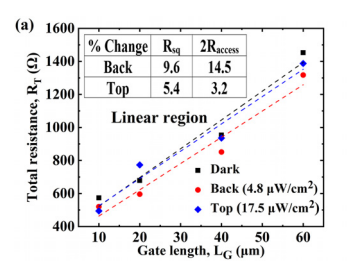
Under illumination, the transfer curve shifted more negative in voltage compared to the dark. This was accompanied by an increase in ID, indicating an increase in the number of electrons in the channel. The maximum absolute persistent photocurrent (PPC) for all the devices was obtained at $\lambda \sim 300$ nm, which is near the band edge of the Al_{0.4}Ga_{0.6}N channel, but well below the band edge of the Al_{0.65}Ga_{0.35}N barrier. The subthreshold swing (SS) of ~200 mV/decade corresponds to an interfacial defect density of $\sim 2 \times 10^{12}$ cm⁻² (Ref. 21) and is unchanged with 300 nm illumination, as well as with the same 365 nm sub-bandgap illumination, which will be shown below to quench the PPC. This indicates that there are no measurable optically active interfacial traps at the barrier/channel interface, implying a high quality Al_{0.65}Ga_{0.35}N/ Al_{0.4}Ga_{0.6}N barrier-channel interface. This was further confirmed by C-V, where no significant change in the characteristic was observed, nor was any hysteresis seen at the channel/barrier 2DEG (supplementary material). Thus, the conducting channel barrier/channel interface cannot be responsible for the slow transient from carrier trapping seen in these devices.

The transient photoresponses of this device with $V_{GS} = -11 \text{ V}$, slightly below V_{th}, are shown in Fig. 1(b). After turning off the 300 nm monochromatic source, the PPC lasting over 10 min in dark ambience, seen in Fig. 1(b), is believed to be associated with the deep traps. This PPC at 300 nm was quenched by \sim 100× from \sim 3 μ A to \sim 25 nA with an additional sub-bandgap flood illumination of 54.8 mW/cm² at 365 nm, while the 10%-90% response time decreased similarly by $\sim 100 \times$ to approximately 0.2 s. The responsivity of $\sim 1.37 \times 10^5$ A/W in the dark was also reduced to $\sim 4.88 \times 10^2$ A/W under 365 nm illumination at $\lambda \sim 300$ nm. A similar quenching of PPC was also seen with an additional 1.58 μ W/cm² 254 nm illumination [Fig. SI2(b)]. The proportional decrease in PPC with the faster response time is a classic signature of photoconductive gain, 16,22 arising from the trapping in sub-bandgap states. Sub-bandgap 365 nm ($hv < E_g$ of $Al_{0.4}Ga_{0.6}N$) light excites deep traps only, whereas the above-bandgap excitation $(hv > E_{\varphi}, \lambda = 300 \,\text{nm} \text{ of Al}_{0.4}\text{Ga}_{0.6}\text{N})$ produces the photoexcitation of deep traps as well as band-to-band generation of electron-hole pairs. We note that both our HFET and AlGaN/GaN control structures also demonstrated similar PPC.

To find the lateral positions of the sub-bandgap traps, a GTLM technique was used as reported earlier for AlGaN/GaN HEMT's. ^23 Moreover, we could bias the device from off to on states using GTLMs, enabling selection of a gate bias that lowers the drain-source channel current to a level that is not influenced by the contact resistance, while still being above V_{th} . We studied the behavior of 300 nm light from both top and back sides in the linear ($V_{\rm DS}=2~V$) region of the output curve on GTLMs for $V_{\rm GS}=-4~V$. The total resistance of a GTLM device, neglecting the contact resistances, $R_{\rm C}$ is given by

$$\begin{split} R_T &= 2R_C + R_{GS} + R_{GD} + R_{CH} \left(L_G \right) \approx 2R_{access} + R_{CH} \left(L_G \right) \\ &= 2R_{access} + R_{sq} \times \left(L_G / W_G \right), \end{split} \tag{1}$$

where R_{GS} and R_{GD} are the resistances of the gate-source and gate-drain access regions and R_{CH} is the gate-length dependent channel resistance for a fixed V_{GS} . In the linear regime, $R_{CH}(L_G) = R_{sq} \times (L_G/W_G)$, where R_{sq} is the sheet resistance under the gate of the device and $2R_{access}$ is the total resistance of the access regions. From a linear plot of R_T vs L_G , R_{sq} is obtained from the slope, while R_{access} is determined from the y-intercept [Fig. 2(a)]. All resistances decreased under both



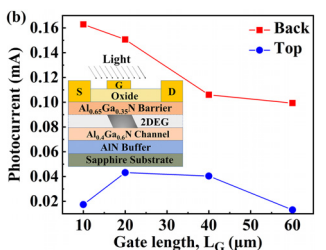
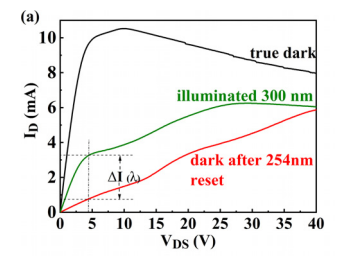


FIG. 2. (a) Gate length dependent total resistance in the linear regime for dark and 300 nm light from back and top sides. (b) Gate length dependent steady-state photocurrent for 300 nm light from back and top sides (Inset: shadow on 2DEG from the opaque metal gate).

top-illumination (17.5 μ W/cm² at 300 nm) and bottom-illumination (4.8 μ W/cm² at 300 nm). With backside illumination, the decrease in R_T is distributed throughout the access (15%) and channel regions (10%), implying that the traps responsible for the observed static photocurrent decreasing R_T are present in both regions. A smaller R_T decrease ~5% was seen with topside illumination, despite the 4× higher 300 nm intensity, demonstrating that shadowing of the incident light by the opaque metal gate [Fig. 2(b)] limited the modulation of R_T and that R_{access} is not strongly modulated from surface illumination. Thus, the topside illumination is intentionally subjected to shadowing in GTLM structures, which enabled us to distinguish potential photoresponse differences between the access region and the channel region. These observations suggest that the sub-bandgap trap states responsible for PPC are located deep enough under the surface, most probably at the AlN/channel growth interface.

Since the GTLM measurements identified the potential location of the trapping effects, photoionization measurements were performed to determine the energy levels of these traps, which were subsequently correlated with the CL spectrum. To maximize the total channel current, and thereby also increasing the photocurrent, the shortest channel length of $L_G=1.8~\mu m$ was used to improve the signal level. This device showed ON/OFF ratio $>10^7$, SS $\approx 110~mV/decade$, and a current drive >0.4~A/mm [Fig. S3(a)], consistent with the GTLM structures described above. Figure 3(a) depicts the $I_D\text{-}V_{DS}$ curve (at a medium sweep rate) in the dark, fully collapsed $I_D\text{-}V_{DS}$ curve in the



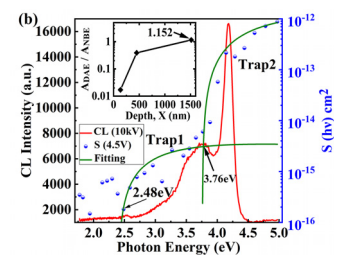


FIG. 3. (a) Output characteristics of the 1.8 μm device with current reduction forced by trapping at high V_{DS}. (b) Overlay of spectral distribution of the response function $S(h\nu)$ with the Lucovsky model fitting and CL spectrum at 10 kV/OFF-mesa (inset: ratio of the defect-assisted emission area, A_{DAE}, to near-band emission area, A_{NBE}, obtained by fitting the Gaussian function for the ON-mesa CL spectra vs beam penetration depth).

dark when 254 nm light is turned off after about 10 min exposure, and the same curve after ${\sim}21$ s under 300 nm illumination since the 254 nm light is removed. The difference between the drain current I_{λ} at λ wavelength and the fully collapsed dark drain current I_{dark} at a fixed $V_{DS}=4.5$ V in the linear regime is the light-induced drain current $\Delta I(\lambda)$ shown in Fig. 3(a). Considering the incident photon flux $\varphi(\lambda)$ for time t, $\Delta I(\lambda)$, and I_{dark} , we plot the spectral dependence of the deep traps utilizing the response function, 17 $S(\lambda)=\frac{1}{\varphi(\lambda)t}\frac{\Delta I(\lambda)}{I_{dark}}$. The measured response function was overlaid with the CL spectrum at 10 kV, as shown in Fig. 3(b), and fit with two trap levels from the Lucovsky model describing the ionization of discrete levels,

$$S(h\nu) = \frac{A_n(h\nu - E_{Tn})^{\frac{3}{2}}}{(h\nu)^3},$$
 (2)

where A_n is a fitting constant and E_{Tn} is the photoionization threshold energy for the nth trap. The best fit to our $S(h\nu)$ data is obtained for $A_1=1.0\times 10^{-13}\, cm^2,~E_{T1}=2.48\pm 0.14~eV~(R^2\sim 0.7)$ and A_2 $= 7.8 \times 10^{-11} \,\mathrm{cm}^2$, $E_{\mathrm{T2}} = 3.76 \pm 0.06 \,\mathrm{eV} \,(\mathrm{R}^2 \sim 0.91)$. There is a small deviation below E_{T1} in the range of 1.5-2.4 eV due to a distribution of this E_{T1} energy level, as has been observed by Klein et al. 17 and from the width of the sub-bandgap CL features ~50 nm. The broad distribution of these states is also supported by the observation of 1/f vs 1/f² noise expected for discrete states.^{24,25} The drain current power spectral density for all the devices exhibited 1/f noise (Fig. S4) in the subthreshold region regardless of the gate length or any lighting conditions. $S(h\nu)$ is thus dominated by the sub-bandgap trap states E_{T1} and E_{T2}, which coincides well with the CL spectrum. This correlation implies that the slow PPC in the device comes from these subbandgap states. The control HFET structure fabricated from the same wafer showed a similar CL signature, while the AlGaN/GaN HEMT control showed defect luminescence similar to Klein et al. in GaN MESFETs.

The traps responsible for PPC have been identified in energy and been assigned to the AlN/channel growth interface from the photoionization and GTLM measurements. This was further underscored by a depth-profiling of the CL spectrum at SEM beam accelerating voltages of 5 kV (\sim 0.134 μ m penetration), 10 kV (\sim 0.45 μ m penetration), and 20 kV (\sim 1.515 μ m penetration).²⁶ By taking the ratio of the area of the defect luminescence peak to that of the band edge luminescence peak [Fig. 3(b), inset], the relative contribution from each vertical location is obtained. In all our devices (MOSHFET, HFET, and AlGaN/ GaN HEMT), the defect peak intensity increased, the deeper the electron beams penetrated (supplementary material), clearly showing that the defects causing the PPC are located at the AlN/channel growth interface. We have recently shown¹³ that silicon nitride passivates the HFET barrier surface precisely for the control HFETs. These passivated HFETs still showed slow transients >10 s similar to that in the MOSHFETs as well as sub-bandgap photoresponse, showing that trapping is still present and does not arise from the surface. However, due to the high gate leakage of the control HFETs arising from a gate contact directly on the doped barrier, 11 it was not possible to quantify the low levels of sub-bandgap photoresponse as with the low leakage in the MOSHFET. Nevertheless, the cathodoluminescence of both the HFET control structure and MOSHFETs (Fig. S5 in the supplementary material) showed similar defect assisted emission that increased with the penetration depth toward the AlGaN channel/AlN growth

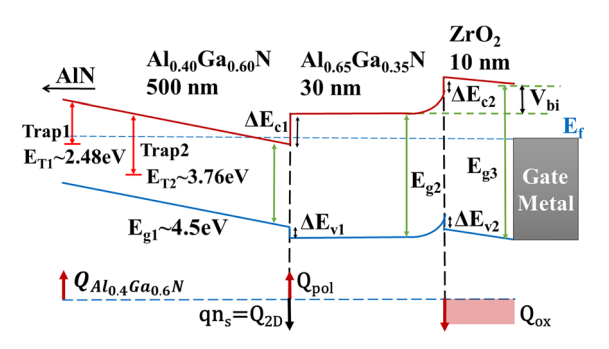


FIG. 4. Equilibrium energy band diagram of the MOSHFET structure with trap locations.

interface. This conclusively shows that the slow trapping does not arise from the surface and is from the growth interface. An equilibrium energy band diagram of the MOSHFET device with trap energies is shown in Fig. 4. The ON-mesa CL spectra for GaN HEMTs have the defect and yellow luminescence as shown in Fig. S5(e). The photoionization threshold energies for GaN MESFETs were 1.8 eV and 2.85 eV compared to 2.48 eV and 3.76 eV for AlGaN/AlGaN MOSHFETs, which are shown in Fig. S7.¹⁷ Accounting for the band-offsets, the trap levels line up for AlGaN and GaN, suggesting that they have the same physical origin. X-ray measurements of that interface show that the Al_{0.4}Ga_{0.6}N layer is epitaxially registered with AlN, with only 10.4% relaxation (supplementary material). Nevertheless, this small relaxation is responsible for the defects seen and plays a significant role in the transient performance of these devices. This relaxation is unavoidable given the large lattice mismatch (\sim 1.6%) at the growth interface. We also note near the barrier/channel interface that, after the \sim 0.5 μ m growth, the traps do not propagate and are localized to the back interface. Therefore, a back barrier geometry is required to electrically isolate the traps from the conduction 2DEG. Solutions include a graded Al composition from 100% down to 40% to induce a isolating polarization field similar to a pn junction or simply a high Al back barrier, which will provide isolation at the expense of lowered 2DEG density. Such back barriers have been used in AlGaN/GaN devices^{27,28} also although the situation is more severe for AlGaN, a truly pseudomorphic geometry, unlike the thicker metamorphic GaN channel layers.

In summary, we have identified the transient performance limiting traps arising from the AlN growth interface in $Al_{0.65}Ga_{0.35}N/Al_{0.4}Ga_{0.6}N$ MOS-HEMTs. These sub-bandgap traps are shown to be quenched optically, and our results suggest that careful back barrier engineering may bring to full fruition the promise of UWBG AlGaN technology for detection applications.

See the supplementary material for the hi-lo C-V curves and D_{it} extraction; transient performance under 254 nm; 1.8 μ m AlGaN MOSHFET transfer curve and GaN HEMT transfer and output curves; 1/f noise in the subthreshold region; ON-mesa, OFF-mesa MOSHFET, and HFET CL spectra and slow transient and ON-MESA CL spectra; Gaussian fitting on the 10 kV/ON-mesa CL spectrum; comparison of trap energies of AlGaN MOSHFETs with GaN MESFETs; and RSLM contour plot of partially relaxed AlGaN material.

This research work was partially supported by the National Science Foundation (NSF), ECCS Award Nos. 1711322 and 1810116 under the supervision of program director Dr. Dimitri Pavlidis. NSF also partially supported this work under Award No. 1831954 under program director Paul Lane. The authors would like to acknowledge partial support of this work by DARPA DREAM contract (No. ONR N00014-18-1-2033), Program Manager Dr. Young-Kai Chen, monitored by ONR, Dr. Paul Maki, and ARO Contract No. W911NF-18-1-0029 monitored by Dr. M. Gerhold. The authors would also like to acknowledge the support from the University of South Carolina through the ASPIRE program. The NRL team also acknowledges support from ONR for their internal funding.

REFERENCES

- ¹J. Y. Tsao, S. Chowdhury, M. A. Hollis, D. Jena, N. M. Johnson, K. A. Jones, R. J. Kaplar, S. Rajan, C. G. Van de Walle, E. Bellotti, C. L. Chua, R. Collazo, M. E. Coltrin, J. A. Cooper, K. R. Evans, S. Graham, T. A. Grotjohn, E. R. Heller, M. Higashiwaki, M. S. Islam, P. W. Juodawlkis, M. A. Khan, A. D. Koehler, J. H. Leach, U. K. Mishra, R. J. Nemanich, R. C. N. Pilawa-Podgurski, J. B. Shealy, Z. Sitar, M. J. Tadjer, A. F. Witulski, M. Wraback, and J. A. Simmons, Adv. Electron. Mater. 4, 1600501 (2018).
- ²M. A. Mastro, A. Kuramata, J. Calkins, J. Kim, F. Ren, and S. J. Pearton, ECS J. Solid State Sci. Technol. **6**, P356 (2017).
- ³M. Su, C. Chen, and S. Rajan, Semicond. Sci. Technol. 28, 74012 (2013).
- ⁴S. Ujita, Y. Kinoshita, H. Umeda, T. Morita, S. Tamura, M. Ishida, and T. Ueda, in 2014 IEEE 26th International Symposium on Power Semiconductor Devices and IC's (IEEE, 2014), pp. 51–54.
- ⁵H. Xue, Q. He, G. Jian, S. Long, T. Pang, and M. Liu, Nanoscale Res. Lett. 13, 290 (2018).
- J. Pearton, F. Ren, M. Tadjer, and J. Kim, J. Appl. Phys. 124, 220901 (2018).
 Nagasawa and A. Hirano, Appl. Sci. 8, 1264 (2018).
- 8S. Muhtadi, S. Hwang, A. Coleman, F. Asif, A. Lunev, M. V. S. Chandrashekhar, and A. Khan, Appl. Phys. Lett. 110, 171104 (2017).
- ⁹T. P. Chow and R. Tyagi, IEEE Trans. Electron Devices **41**, 1481 (1994).

- ¹⁰S. Muhtadi, S. M. Hwang, A. Coleman, F. Asif, G. Simin, M. V. S. Chandrashekhar, and A. Khan, IEEE Electron Device Lett. 38, 914 (2017).
- ¹¹X. Hu, S. Hwang, K. Hussain, R. Floyd, S. Mollah, F. Asif, G. Simin, and A. Khan, IEEE Electron Device Lett. 39, 1568 (2018).
- ¹²S. Mollah, M. Gaevski, M. V. S. Chandrashekhar, X. Hu, V. D. Wheeler, K. Hussain, A. Mamun, R. Floyd, I. Ahmad, and G. Simin, Semicond. Sci. Technol. 34, 125001 (2019).
- ¹³S. Mollah, M. Gaevski, K. Hussain, M. Abdullah, R. Floyd, X. Hu, M. V. S. Chandrashekhar, G. Simin, and A. Khan, Appl. Phys. Express 12, 074001 (2019).
- 14T. Narita, A. Wakejima, and T. Egawa, Jpn. J. Appl. Phys., Part 1 52, 01AG06 (2013)
- ¹⁵C. V. Reddy, K. Balakrishnan, H. Okumura, and S. Yoshida, Appl. Phys. Lett. 73, 244 (1998).
- ¹⁶J. Z. Li, J. Y. Lin, H. X. Jiang, and M. A. Khan, Appl. Phys. Lett. **72**, 2868 (1998).
- ¹⁷P. B. Klein, J. A. Freitas, S. C. Binari, and A. E. Wickenden, Appl. Phys. Lett. 75, 4016 (1999).
- ¹⁸Q. Fareed, V. Adivarahan, M. Gaevski, T. Katona, J. Mei, F. A. Ponce, and A. Khan, Jpn. J. Appl. Phys., Part 2 46, L752 (2007).
- ¹⁹C. Pernot, M. Kim, S. Fukahori, T. Inazu, T. Fujita, Y. Nagasawa, A. Hirano, M. Ippommatsu, M. Iwaya, and S. Kamiyama, Appl. Phys. Express 3, 61004 (2010)
- ²⁰J.-S. Park, J. K. Kim, J. Cho, and T.-Y. Seong, ECS J. Solid State Sci. Technol. 6, Q42 (2017).
- ²¹P. H. Carey, F. Ren, A. G. Baca, B. A. Klein, A. A. Allerman, A. M. Armstrong, E. A. Douglas, R. J. Kaplar, P. G. Kotula, and S. J. Pearton, IEEE J. Electron Devices Soc. 7, 444 (2019).
- ²²M. T. Hirsch, J. A. Wolk, W. Walukiewicz, and E. E. Haller, Appl. Phys. Lett. 71, 1098 (1997).
- ²³G. Simin, A. Koudymov, A. Tarakji, X. Hu, J. Yang, M. A. Khan, M. S. Shur, and R. Gaska, Appl. Phys. Lett. **79**, 2651 (2001).
- ²⁴F. N. Hooge, IEEE Trans. Electron Devices **41**, 1926 (1994).
- ²⁵M. J. Deen, S. L. Rumyantsev, and M. Schroter, J. Appl. Phys. **85**, 1192 (1999).
- ²⁶T. E. Everhart and P. H. Hoff, J. Appl. Phys. **42**, 5837 (1971).
- ²⁷T. Palacios, A. Chakraborty, S. Heikman, S. Keller, S. P. DenBaars, and U. K. Mishra, IEEE Electron Device Lett. 27, 13 (2006).
- ²⁸G. Simin, X. Hu, A. Tarakji, J. Zhang, A. Koudymov, S. Saygi, J. Yang, A. Khan, M. S. Shur, and R. Gaska, Jpn. J. Appl. Phys., Part 2 40, L1142 (2001).